A Computational Study of the Deacylation Mechanism of Human Butyrylcholinesterase†

Dimas Suárez,*,‡ Natalia Díaz,‡ Juan Fontecilla-Camps,§ and Martin J. Field||

Departamento de Química Física y Analítica, Universidad de Oviedo, Julián Clavería 8, 33006 Oviedo, Spain, Laboratoire de Cristallographie et Cristallogenèse des Protéines, Institut de Biologie Structurale—Jean-Pierre Ebel, CEA/CNRS 41, rue Jules Horowitz, F-38027 Grenoble Cedex 1, France, and Laboratoire de Dynamique Moléculaire, Institut de Biologie Structurale—Jean-Pierre Ebel, CEA/CNRS 41, rue Jules Horowitz, F-38027 Grenoble Cedex 1, France

Received October 25, 2005; Revised Manuscript Received April 17, 2006

ABSTRACT: To investigate the mechanism of the deacylation reaction in the active site of human butyrylcholinesterase (BuChE), we carried out quantum mechanical (QM) calculations on cluster models of the active site built from a crystallographic structure. The models consisted of the substrate butyrate moiety, the catalytic triad of residues (Ser_{198}, Glu_{325}, and His_{438}), the "oxy-anion hole" (Gly_{116}, Gly_{117}, and Ala_{199}), the side chain of Glu_{197}, four water molecules, the side chain of Ser_{225}, and the peptide linkage between Val_{321} and Asn_{322}. Analyses of the equilibrium geometries, electronic properties, and energies of the QM models gave insights into the catalytic mechanism. In addition, the QM calculations provided the data required to build a molecular mechanics representation of the reactive BuChE region that was employed in molecular dynamics simulations followed by molecular-mechanics−Poisson−Boltzmann (MM−PB) calculations. Subsequently, we combined the QM energies with average MM−PB energies to estimate the free energy of the reactive structures in the enzyme. The rate-determining step corresponds to the formation of a tetrahedral intermediate with a free-energy barrier of ∼14.0 kcal/mol. The modulation of the BuChE activity, exerted by either neutral molecules (glycerol, GOL) or a second butyrylcholine (CHO) molecule bound to the cation−π site, does not involve any significant allosteric effect. Interestingly, the presence of GOL or CHO stabilizes a product complex formed between a butyric acid molecule and BuChE. These results are in consonance with the crystallographic structure of BuChE, in which the catalytic Ser_{198} interacts with a butyric fragment, while the cation−π site is occupied by one GOL molecule.

Cholinesterases are members of the family of hydrolases (*1*, *2*). In vertebrates, there are two cholinesterases, acetylcholinesterase (AChE)[1] and butyrylcholinesterase (BuChE), which differ in their catalytic properties, inhibition patterns, and tissue distributions and which share 53% sequence homology. The principal role of AChE is in the nervous system, where it serves to terminate impulse transmission at cholinergic synapses by hydrolysis of the neurotransmitter acetylcholine at nearly diffusion-limited rates (*3*). It occurs mainly in a glycophospholipid-linked form that is membrane-associated and can exist as monomers and dimers. BuChE, which is also named serum cholinesterase, is widely distributed in tissues and plasma although a clear physiological role has not been ascribed. Nevertheless, the BuChE enzyme is of interest to anesthesiologists and geneticists because it is responsible for the breakdown of the short-term muscle relaxant succinyldicholine and because numerous genetic variants of BuChE exist with lower affinity for succinyldicholine (*4*). BuChE is also a major detoxifying enzyme because it hydrolyzes drugs such as cocaine (*5*) or scavenges organophosphorus pesticides and chemical warfare agents (*6*). Moreover, it has been reported that BuChE catalyzes the hydrolysis of acetylcholine in the nervous system and thus could serve as a coregulator of cholinergic transmission (*7*, *8*).

In accordance with X-ray crystallographic studies (*9*, *10*), the overall architecture of the AChE and BuChE enzymes is quite similar. The active site is located at the bottom of a deep cavity named the "aromatic gorge" because its surface is lined by the rings of 8 aromatic residues in BuChE and by those of 14 in AChE. In the crystallographic structure of AChE, the channel leading from the surface to the catalytic cavity is so narrow that substrate molecules cannot access the active site, whereas the channel and gorge cavity in the BuChE structure are much less confining (*10*, *11*). The

† D.S. acknowledges EMBO and EGIDE (France) for their short-term grants ASTF-98-02 and 371237-L-2003, respectively.

* To whom correspondence should be addressed. Telephone: +34-985182266. Fax: +34-985103125. E-mail: dimas@uniovi.es (D.S.); Telephone: +33-4-38-78-99-28. Fax: +33-4-38-78-54-94. E-mail: mjfield@ibs.fr (M.J.F.).

‡ Universidad de Oviedo.

§ Laboratoire de Cristallographie et Cristallogenèse des Protéines, Institut de Biologie Structurale—Jean-Pierre Ebel.

|| Laboratoire de Dynamique Moléculaire, Institut de Biologie Structurale—Jean-Pierre Ebel.

[1] Abbreviations: B3LYP, Becke 3 Lee−Yang−Parr; AChE, acetylcholinesterase; DFT, density functional theory; BuChE, butyrylcholinesterase; MD, molecular dynamics; BTY, butyrate; MM, molecular mechanical; CHO, butyrlcholine; PB, Poisson−Boltzmann; GOL, glycerol; PES, potential energy surface; PDB, Protein Data Bank; QM, quantum mechanical; QM/MM, hybrid quantum mechanical and molecular mechanical; ZPVE, zero-point vibrational energy.

10.1021/bi052176p CCC: $33.50
Published on Web 05/19/2006

cholinesterases possess a catalytic triad of residues in their active site (Glu_{325}, His_{438}, and Ser_{198}; BuChE residue numbering), which closely resembles that of serine proteases (*12*). When a substrate molecule is complexed in the deep catalytic site, it is commonly thought that the Ser hydroxyl group is the nucleophile that attacks the substrate carbonyl group to give an acyl−enzyme intermediate. Subsequently, a water molecule deacylates the Ser residue by hydrolyzing its ester linkage to the substrate. In both mechanistic steps, the Glu−His pair is crucial in activating the nucleophile and in donating the proton to the leaving group.

Three binding subsites contribute to properly orienting the choline ester substrates in the catalytic cavity. Using BuChE residue numbers, these are (1) a three-pronged "oxy-anion hole" formed by the backbone amides of Gly_{116}, Gly_{117}, and Ala_{199} that stabilizes the negative charge developed at the carbonylic O atom of the substrate in the acylation/deacylation process, (2) the aromatic rings of Trp_{82} and Phe_{329} that stabilize the quaternary ammonium function of the choline moiety through cation−π interactions, and (3) a concave hydrophobic pocket (the acyl-binding pocket) consisting of residues Trp_{230}, Phe_{329}, Leu_{286}, and Val_{288} (the two latter residues are situated in the so-called acyl loop), in which the propanoyl (or acetyl) function of the substrate is bound.

The catalytic mechanism of BuChE has been investigated intensively by means of mutagenesis and kinetic experiments using different substrate molecules [butyrylthiocholine (BTC), succinyldithiocholine, etc.] (*4*, *13*−*16*). These studies have shown that the deacylation step is most likely rate-determining at low substrate concentrations. The kinetic studies also revealed that the BuChE enzyme exhibits a complex kinetic behavior. Thus, the hydrolysis of BTC by wild-type BuChE exhibits three distinct kinetic phases depending upon the concentration of BTC (*16*). The first phase, in which kinetic data fit well to a Michaelis equation, is observed in the 0.01−0.10 mM range (*13*). In the second phase, from 0.4 to 40 mM, there is a 2.5−3-fold increase in the turnover number of the BuChE enzyme in the presence of excess substrate. This substrate activation is generally considered to be a defining property of BuChE, in contrast to AChE, which shows substrate inhibition. In the third phase, when the BTC concentration is over 40 mM, the kinetic behavior of BuChE displays substrate inhibition.

On the basis of kinetic data and molecular-modeling results, it has been proposed that the peculiar kinetic properties of BuChE are most likely induced by excess substrate molecules bound to the so-called "peripheral" and "intermediate" sites, whose existence has been confirmed by the X-ray structures of BuChE complexed with BTC or soman (*10*). The peripheral site is located at the rim of the aromatic gorge and contains the residue Asp_{70}, which presumably plays an important role in stabilizing and orienting the excess substrate molecules. The intermediate site is located near the bottom of the gorge channel, where the indole group of Trp_{82} interacts with the positively charged choline head of substrate molecules to give a cation−π complex. It must be noted, however, that the subtle molecular details through which the excess substrate molecules can affect the hydrolysis reaction of the substrate molecule bound to the catalytic cavity remain to be elucidated.

Other striking features of cholinesterases manifested in their crystallographic structures are (a) their ability to bind neutral molecules (polyethylene gylcol and glycerol), at the cation recognition site through interactions that structurally mimic the cation−π interactions formed in substrate binding (*10*, *17*), and (b) the presence of electron-density peaks very close to the catalytic Ser residue that can be modeled as small anionic molecules (carbonate and sulfate) (*18*, *19*). In addition, in the crystallographic structure of native BuChE at 2.0 Å, the electron-density peak adjacent to the Ser_{198} residue was best modeled as a tetrahedral butyryl group bound to Ser_{198} with a Ser_{198} Oγ···C butyryl distance of 2.16 Å (*10*). Several lines of evidence confirm this interpretation because further experimental work has shown that (a) 3-bromopropionate, when used to replace butyrate, is found in this position, (b) the moiety is displaced by choline, and (c) the presence of butyrate turned out to be essential for crystrallization because butyrate-depleted BuChE samples are extremely difficult to crystallize (*10*). The presence of a putative butyrate bound to Ser_{198} is also sterically compatible with substrate binding at the intermediate site by analysis of the X-ray structure of the soman-aged BuChE−BTC complex. All of these results suggest that binding of butyrate to the Ser_{198} hydroxyl group could be somehow related to the reactivity and/or stability of the catalytic serine. Hence, it has been proposed that concerted product release/substrate binding at a deprotonated Ser_{198} could be a mechanistic alternative to the expected activation of Ser_{198} by the nearby His_{438} (*10*).

Most of the previous theoretical work on the catalytic mechanism of cholinesterases has been carried out on the AChE enzyme to understand the origin of its remarkable rate enhancement ($\sim 10^{13}$) (*20*−*23*). The most consistent simulation studies of the acylation and deacylation pathways have been performed by Fuxreiter et al. (*24*) and Vagedes et al. (*25*). These workers evaluated the activation free energies for the reactions using an empirical valence bond (EVB) potential energy function that included long-range electrostatic and solvent effects in combination with all-atom free-energy perturbation (FEP) calculations. These EVB/FEP calculations showed that the AChE enzyme reduces the activation energy barriers for the acylation/deacylation steps by 10−15/11−12 kcal/mol relative to reference reactions in water. These important catalytic effects were mainly due to the electrostatic forces exerted by the catalytic triad and adjacent residues (the "oxy-anion hole" and the acidic Glu_{197} residue in BuChE residue numbering). For the acylation reaction, the attack of the nucleophilic hydroxyl group of Ser_{198} is concomitant with a single proton transfer (Ser-OH ← :Nϵ-His), while the Glu residue in the catalytic triad and the "oxy-anion" hole are essential in stabilizing the transition structure and the tetrahedral intermediate along the reaction pathway through electrostatic interactions (*24*, *25*).

Other workers have also studied various aspects of the reactions catalyzed by AChE and BuChE. Thus, for example, Zhang et al. investigated the acylation step of the AChE reaction using a hybrid quantum mechanical/molecular mechanical (QM/MM) method in combination with reaction path calculations. These estimated the average energy barrier for the acylation step to be 13.0 kcal/mol, although long-range electrostatic and solvent effects were not taken into account (*26*, *27*). Likewise, Zhan et al. have addressed the

reaction mechanisms of hydrolysis of (+)- and (−)-cocaine by BuChE using QM calculations on small cluster models (*28*) and ONIOM calculations on BuChE−cocaine complexes (*29*). Both of these techniques neglect or fail to account properly for the interactions between the active-site atoms and the surrounding protein and solvent.

Clearly, the availability of BuChE crystallographic structures poses interesting questions regarding the catalytic mechanism of the cholinesterases. What is the catalytic relevance of the presence of the butyrate moiety detected crystallographically? What is the nature of the interaction between the butyrate and Ser_{198}? Can neutral molecules bound to the cation−π site affect catalysis? How does a second substrate molecule influence the kinetics? These and other questions are amenable to analysis by means of theoretical calculations and, therefore, in this paper, we have investigated the deacylation process of the BuChE enzyme, which is most likely the rate-determining step in the catalytic cycle. We carried out extensive QM calculations on large and realistic cluster models of the active site built from the X-ray coordinates and took into account protein and solvent effects on the reaction profile by means of molecular dynamics (MD) simulations followed by molecular mechanics and Poisson−Boltzmann (MM−PB) free-energy calculations. Subsequently, we combined QM energies with average MM−PB free energies to estimate the free energy of reactive structures with respect to the precursor acyl−enzyme complex. Altogether, these theoretical results complement well the X-ray data and give insight into substrate binding and catalysis of the BuChE enzyme.

MATERIALS AND METHODS

Quantum Chemical Calculations on Cluster Models. Starting coordinates for the cluster models of the active site were taken from the crystallographic structure of the recombinant and truncated human BuChE at 2.0 Å resolution [Protein Data Bank (PDB) ID code 1P0I] (*10*). The models consisted of the butyrate moiety observed in the crystal structure, the catalytic triad of residues (Ser_{198} and the side chains of Glu_{325} and His_{438}), the "oxy-anion" hole (Gly_{116}, Gly_{117}, and Ala_{199}), the side chain of Glu_{197}, four water molecules, the side chain of Ser_{225}, and the peptide linkage between Val_{321} and Asn_{322}, giving a total of 112 atoms. We note in passing that inclusion of the side chain of Ser_{225} and the Val_{321}−Asn_{322} peptide bond in the cluster model turned out to be essential to preserve the orientation of the catalytic triad close to that observed in the X-ray structure.

To prevent movement of groups of atoms to locations unattainable in the actual BuChE system, the cluster models were optimized with constraints. For the amino acid moieties included in the QM models, constraints were imposed by including the three closest backbone heavy atoms as non-QM dummy atoms. These atoms constituted the first three atoms in a *Z*-matrix input for each fragment, and all bonds, angles, and dihedrals formed with these dummy atoms were fixed. In addition, torsional constraints were imposed along the Gly_{116}−Gly_{117} moiety. We note, however, that the QM model retained sufficient flexibility.

The internal geometry of the cluster models was relaxed using the Becke 3 Lee−Yang−Parr (B3LYP) functional (*30*) with the double-ζ 6-31G* basis set using the Jaguar program giving a total of 980 basis functions (*31*). Geometry optimizations at the B3LYP/6-31G* level used a Broyden−Fletcher−Goldfarb−Shanno (BFGS) minimizer until the maximum force and the root-mean-square (rms) force were below 0.001 and 0.0003 au, respectively. To locate transition structures on the potential energy surface (PES), we employed the synchronous transit quasi-Newton method implemented in Jaguar. To characterize the critical structures located on the B3LYP/6-31G* PES, we carried out analytical Hessian calculations on the optimized structures using the Gaussian03 suite of programs (*32*). In addition, zero-point vibrational energy (ZPVE) corrections were computed using the B3LYP/6-31G* Hessian matrices. To avoid any contribution of the residual gradient (because of the internal constraints) to the ZPVE corrections, we diagonalized submatrices of the corresponding full Hessian matrices. These were constructed by taking the matrix elements associated with the nuclear degrees of freedom from the butyrate moiety, the Ser_{198}, Glu_{197}, and His_{438} side chains, and four water molecules. After geometry optimization, the electronic energies for all of the structures were refined by means of single-point calculations using the 6-311+G(d,p) basis set and Gaussian03. As an initial estimate of the effect of the protein and solvent environment on the different critical structures, we performed single-point self-consistent reaction field (SCRF) calculations on the gas-phase QM geometries using the PB solver (*33*) included in Jaguar. Several values for the dielectric constant of the surrounding continuum (ϵ) were considered to analyze the trend in the relative solvation energies: 80 (water, high polarity), 20 (intermediate polarity), and 4 (low polarity).

For comparative purposes, we also studied the donor−acceptor interaction between one water molecule and one acetic acid molecule. Geometry optimizations were done at the MP2/6-31G*, MP2/6-311+G(2d,2p), B3LYP/6-31G*, and B3LYP/6-311+G(2d,2p) levels of theory. Single-point CCSD(T)/6-311+G(2d,2p) calculations were also carried out at the MP2/6-311+G(2d,2p) geometries. All of these calculations were performed using Gaussian03.

Using Bader's theory of atoms in molecules (*34*), the nature of the Ser_{198} Oγ···C butyryl bond and the water··· acetic acid interaction were further analyzed by calculating the corresponding bond critical point (BCP) properties in the charge density $\rho(r)$. The values of $\rho(r)$, $\nabla^2\rho(r)$, and of the local energy density $H(r)$ at the BCPs enable one to characterize the interatomic interactions. The BCP analysis employed the EXTREME program, a part of the AIMPAC suite of programs (*35*).

Environmental Effects: Combining QM, PB, and MM Calculations. We sought to estimate free-energy profiles for the BuChE reaction in the presence or absence of different molecules in the gorge and active site, in particular, a Na^+ cation, a glycerol (GOL) molecule, or a second butrylcholine molecule. To fulfill this goal, we needed to take into account long-range electrostatic effects as well as the structural fluctuations of the surrounding protein and solvent environments. In principle, FEP calculations of the fully solvated enzyme−substrate complex carried out with a hybrid QM/MM Hamiltonian could have provided the required free-energy profiles, but such QM/MM FEP calculations would have been rather difficult to converge and clearly prohibitive in terms of computational cost.

In addition to FEP calculations, environmental effects on the energy profiles could have been estimated by combining a classical force field with the so-called "semimicroscopic" version of the protein dipoles−Langevin dipoles method (*36*) (PDLD/S) that has been used in the study of the acylation step of AChE (*24*). In this approach, the PDLD/S free energies for individual enzyme configurations are treated in the framework of the linear response approximation. This means that solvation free-energy contributions to the PDLD/S free energies are averaged over the enzyme configurations generated with two MD simulations, one with the actual charge distribution and the other with a zero-charge distribution. In this work, however, we followed a simplified approach in which the PDLD method is replaced by the PB method, only one MD simulation is carried out to generate the statistical ensemble of enzyme−substrate structures, and the AMBER force field is used to represent the enzyme−substrate models. This approach can be considered a variant of the so-called MM−PB approach (*37*) that has been widely applied for calculating enzyme−substrate, protein−protein, and DNA−protein binding free energies (*38*). For this reason, the computational approach used in this work is referred to as the MM−PB method.

To apply the proposed MM−PB approach, we first derived MM representations for the reactive regions of the BuChE−butyrate complex that were built from the QM critical structures located along the reaction path. Then, we combined QM energies with average MM−PB free energies to estimate the free energy of reactive structures [transition structures (TSs), tetrahedral intermediate, and product complexes] with respect to the precursor (reactant) acyl−enzyme complex. Thus, for example, the relative free energy of a TS structure in the enzyme was estimated by the following equation:

$$\Delta G = E_{QM}^{cluster}(TS) - E_{QM}^{cluster}(reactant) + \Delta\Delta G^{enviroment} \quad (1)$$

where the E_{QM} terms are the QM energies of the corresponding TS and reactant cluster models and $\Delta\Delta G^{enviroment}$ represents the average environmental correction to ΔE_{QM} that is obtained through the following expression:

$$\Delta\Delta G^{enviroment} = \bar{G}_{MMPB}^{enzyme}(TS) - \bar{G}_{MMPB}^{enzyme}(reactant) + \bar{E}_{MM}^{cluster}(reactant) - \bar{E}_{MM}^{cluster}(TS) \quad (2)$$

where the $\bar{G}_{MMPB}^{enzyme}$ terms are the average MM−PB free energies of the corresponding TS and reactant enzyme−substrate complexes, which differ in their MM representations of the reactive region. Similarly, the $\bar{E}_{MM}^{cluster}$ terms are the MM energies of the TS and reactant cluster models.

The average free-energy terms (G_{MMPB}) in eq 2 are computed by combining MM and electrostatic calculations

$$\bar{G}_{MMPB} = \bar{E}_{MM} + \bar{G}_{PB} \quad (3)$$

where $\bar{E}_{MM}$ is the average MM energy

$$\bar{E}_{MM} = \bar{E}_{bond} + \bar{E}_{angle} + \bar{E}_{tors} + \bar{E}_{vdW} + \bar{E}_{elec} \quad (4)$$

These terms correspond to the bond, angle, torsion, van der Waals, and electrostatic terms in the AMBER force field, respectively (*39*). $\bar{G}_{PB}$ in eq 3 is the solvation free energy obtained by PB electrostatic calculations (*40*). Note that eq 2 avoids counting the MM terms affecting the atoms in the cluster model and that harmonic entropic contributions of the surroundings are not taken into account.

When the MM−PB method is applied to estimate the ΔG for ligand−protein association (i.e., $\Delta G = \bar{G}_{complex} - \bar{G}_{protein} - \bar{G}_{ligand}$), the required G terms are usually evaluated over a series of representative (50−100) snapshots from a single MD trajectory of the complex ("one trajectory" approximation) (*37*). Analogously, for each BuChE molecular environment considered in this work, we performed a single MD simulation to generate protein and solvent structures that were compatible with the geometry and charge distribution of the QM cluster models. These, in turn, provided the data required to build the MM models of the reactive region in BChE. In the MD simulations, we employed the locally enhanced sampling (LES) technique (*41*, *42*), which allows the selective application of additional computational effort to a portion of the system, increasing the sampling of the region of interest (i.e., the reacting region of BuChE represented by the QM cluster model). The enhanced sampling is achieved by replacing the region of interest with multiple copies. These copies are constructed in a special way: they do not interact with each other and interact with the rest of the system in an average way. The usual implementation of the LES algorithm assumes that all of the copies share the same topology (i.e., the same covalent structure). In our approach, however, each LES copy corresponded to a MM model coming from a QM structure with a particular topology and set of atomic charges. In addition, we constrained the internal geometry of the LES copies by adding a harmonic energy term computed from the rms coordinate deviations (rmsd) between each copy in the simulation and its reference QM geometry.

Setting Up the BuChE−Butyrate Models for the MD−LES and MM−PB Calculations. Some details of the molecular manipulations, the MD−LES simulations, and the MM−PB calculations that were required to compute the $\Delta\Delta G^{environment}$ terms in eq 2 are as follows:

First, we edited the large cluster models optimized at the B3LYP/6-31G* level by removing the coordinates of the atoms representing the three nonreactive water molecules, the side chain of Ser_{225}, and the peptide linkage between Val_{321} and Asn_{322}. This reduction in size was done to ensure that the BuChE environment around the rigid reactive region was fully flexible during the MD−LES simulations (see below). The energy of these QM substructures (denoted as "small QM models" hereafter) was computed by means of single-point HF/6-31+G* and B3LYP/6-311+G** calculations. From each small QM model, we built a MM model of the reactive region in BuChE (denoted the "reactive MM model"). Atomic partial charges for the reactive MM models were derived from the HF/6-31+G* electrostatic potential of the corresponding small QM models using the RESP methodology (*43*). The RESP fitting procedure allowed us to assign a 0 value to the atomic charges of the hydrogen link atoms and to fix the net charge of selected groups of QM atoms to their equivalent values in the standard AMBER database (Gly_{116}−Gly_{117} to 0.0986 *e*, Ser_{198}(backbone)−Ala_{199} to −0.0986 *e*, Glu_{325} to −1.0 *e*, Glu_{197} to −1.0 *e*, and the butyrate−His_{438}−Ser_{198}(side chain) moiety to 0.0 *e*). In this way, we made sure that electrostatic interactions between all atoms of the enzymatic system are treated on an equal

basis, thereby minimizing partial charge artifacts in the MM−PB calculations. Atom types for the "reactive MM models" were taken from the closest existing AMBER atom types.

To build the solvated BuChE−butyrate systems, we extracted one snapshot from our previous MD simulation of the native form of the BuChE enzyme in aqueous solution (*44*). Then, we docked a "reactive MM model" along the reaction profile (the tetrahedral intermediate, int, see below) into the BuChE active site. Besides considering the native form of BuChE, we also modified the molecular environment within the BuChE gorge through model building. In this way, we set up four different configurations of the BuChE−butyrate system: BCHE−BTY (BuChE complexed with the butyrate), BCHE−BTY−Na^+ (BuChE−butyrate complex in the presence of the gorge Na^+ ion), BCHE−BTY−GOL (BuChE−butyrate complex with one GOL molecule replacing three gorge water molecules), and BCHE−BTY−CHO (BuChE−butyrate complex in the presence of a butyrylcholine (CHO) molecule bound to the intermediate site).

For each enzymatic configuration (BCHE−BTY, BCHE−BTY−Na, BCHE−BTY−GOL, and BCHE−BTY−CHO), the active-site region was partially relaxed through MM energy minimization. Subsequently, a 500 ps MD simulation was carried out for equilibration with protocols identical to those previously used for the native form of BuChE: the protein and solvent atoms were represented by the parm94 version of the AMBER force field; periodic boundary conditions were applied; constant pressure and temperature were controlled by Berendsen's algorithm; and long-range interactions were treated with the Particle-Mesh-Ewald method. Further details are given in our previous paper (*44*). Most atoms in the reactive MM model (int) were forced to maintain their internal (QM) geometry by the imposition of harmonic rmsd constraints. The exceptions were the atoms of the $CH_3CH_2CH_2-$ tail of the butyrate moiety, which were allowed to move freely. After the 500 ps MD simulation, a 1.0 ns LES−MD simulation was carried out with three different LES copies of the "reactive MM models": a prereactive structure (acyl), the tetrahedral intermediate (int), and a product complex (prodA). The geometry of each LES copy was linked to its corresponding QM reference structure by again applying appropriate rmsd constraints. All of the MD trajectories were computed with the SANDER module of the AMBER 7.0 package of programs (*45*).

A total of 100 snapshots were extracted from the last 500 ps of each LES−MD trajectory. The snapshots were processed before carrying out the MM−PB calculations by removing the counterions and most of the water molecules. Only the ~50 water molecules within the gorge cavity were kept because these interact directly with the protein residues and the reacting butyrate moiety. The coordinates of the LES copies were replaced by those of the reactive MM models along the energy profile. In this way, we generated six different structures, differing only in the coordinates of the reactive MM model, from a single MD−LES snapshot. This task was accomplished by rigid superposition of the different reactive MM models onto selected backbone atoms of the MD−LES snapshot, followed by partial MM relaxation of the explicit solvent molecules (including Na^+, GOL, or CHO) and some protein atoms situated at the covalent linkages between the reactive MM models and the rest of the system.

The MM and PB calculations were done with AMBER charges for the different models. All of the MM energies were computed with no cutoff using the SANDER program. The PB calculations were carried out with the program Delphi (*46*, *47*), solving the linearized PB equation on a cubic lattice by using an iterative finite-difference method (1000 iterations) and a grid spacing of 0.5 Å ($200 \times 200 \times 200$). Because of the small size of hydrogens in the AMBER force field, the van der Waals surface used in the PB calculations was constructed using DREIDING van der Waals radii for C, H, N, O, and S atoms (*48*). The dielectric boundary was the contact surface between the radii of the solute and the radius (1.4 Å) of a water probe molecule. The Debye−Hückel approximation was used to determine the potentials at the boundary of the grid.

Validation Calculations. In the Supporting Information, we present a series of test calculations supporting the use of the MD−LES and MM−PB computational protocol for studying environmental effects on the BuChE deacylation reaction. We show first the convenience of carrying out an MD−LES simulation for configurational sampling prior to the MM−PB calculations instead of carrying out standard MD simulations. In addition, we explore the sensitivity of the MM−PB method to the level of theory (HF/6-31+G* or B3LYP/6-31+G*) employed for the derivation of the RESP charges in the gas phase and show that the results are robust regardless of the method. We also compare the effect of gas-phase versus condensed-phase charges (SCRF) on the MM−PB calculations and find that mixing condensed-phase charges for the "QM models" and gas-phase charges for the surrounding environment gives an unbalanced description of the electrostatic interactions.

We also investigate the intramolecular S_N2 reaction in water of a phenol succinate monoester to give a cyclic anhydride and phenolate anion. This reaction can be considered as a reference reaction for the enzymatic hydrolysis of the acyl−enzyme intermediate catalyzed by the BuChE enzyme. We find that the MD−LES simulations of the reactive configurations of the succinate monoester followed by MM−PB calculations predict relative solvation energies very similar to those computed by standard QM SCRF calculations. Finally, we study the conversion of (−)-chorismate to prephenate catalyzed by chorismate mutase using QM, MD−LES, and MM−PB calculations. Our value for the free-energy barrier in the chorismate mutase enzyme amounts to 13.7 kcal/mol, which compares reasonably well with the experimental value of 15.4 kcal/mol. Overall, we conclude that the combination of MD−LES simulations with MM−PB calculations can give a balanced description of environmental effects on enzymatic processes or intramolecular reactions in solution.

Parametrization of Glycerol and Butyrylcholine. Initial coordinates for GOL and CHO were built by molecular modeling. Five low-lying conformers of CHO differing in the N^+−C-C−O and C−C−O−C dihedral angles (namely, the TT, TG, GG, G*G, and GT conformers), were optimized at the HF/6-31G* level in the gas phase followed by single-point MP2/6-31+G** energy calculations. The RESP charge model for CHO was derived using the electrostatic potential of the five CHO conformers. Similarly, four rotational conformers of GOL from the optimized HF/6-31G* PES were employed to derive the set of RESP charges for GOL.

Table 1: B3LYP/6-31G*-Optimized Structures for the Deacylation of the Butyrate−BChE Complex[a]

structure	B3LYP/ 6-31G*	ZPVE[c]	B3LYP/ 6-311+G**[b]	$\Delta\Delta G_{solv}$ B3LYP/6-31G* SCRF[b] $\epsilon = 80$	$\epsilon = 20$	$\epsilon = 4.0$
acyl	0.0	0.0	0.0	0.0	0.0	0.0
TS1	6.0	−2.3	10.4	0.2	0.1	0.0
int	3.7	0.0	9.2	−4.5	−4.0	−2.8
TS2	15.7	−3.5	19.4	−3.4	−3.1	−2.2
prodA	11.1	−0.9	12.5	−3.6	−3.3	−2.3
TS3	12.3	−3.5	13.4	−3.0	−3.1	−3.2
prodB	−19.1	0.1	−14.6	2.3	2.3	1.5

[a] Relative energies are in kcal/mol. [b] Single-point calculations at the B3LYP/6-31G* geometries. [c] From B3LYP/6-31G* frequencies.

Scheme 1

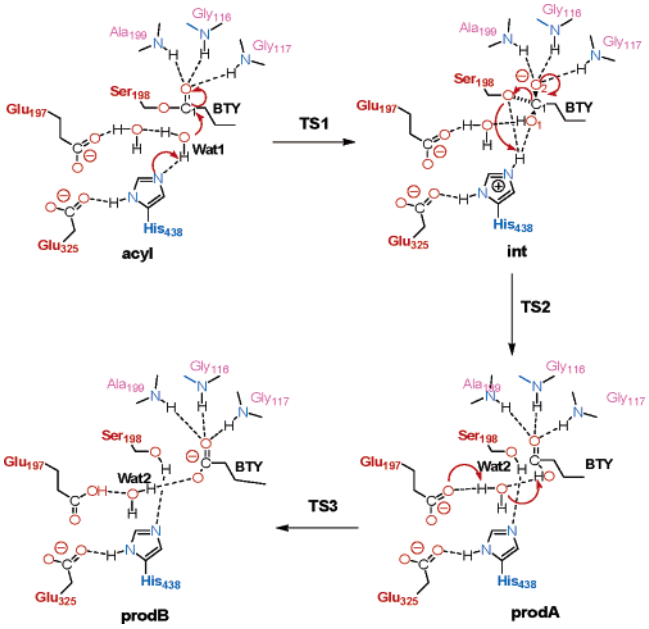

For the two molecules, most of the bond, angle, and dihedral parameters were available from the AMBER force field. The van der Waals (vdW) parameters were taken from the closest existing AMBER atom types chosen according to electronic structure similarity. In addition, some specific torsion parameters were adjusted to reproduce the MP2/6-31+G**//HF/6-31G* relative energies among the conformers. The resulting GOL and CHO parametrizations were tested by minimizing the geometry of their respective conformers, with the resultant MM equilibrium structures being similar to the HF/6-31G* ones. In terms of energies, the AMBER ΔE terms were in good agreement with the ab initio data. The MM parameters for GOL and CHO are reported in the Supporting Information.

RESULTS AND DISCUSSION

QM Calculations: Reaction Pathway. Scheme 1 represents the reaction mechanism for the deacylation process according to our B3LYP/6-31G* calculations on the cluster model of the acylated BuChE active site. Table 1 contains the relative energies of the corresponding critical points with respect to the initial acyl−enzyme structure, while the values of important interatomic distances along the reaction coordinate are included in Table 2. Views of all of the critical structures are included in Figure S1 in the Supporting Information.

The reaction mechanism starts at an acyl−enzyme structure (acyl) that is attacked by the nucleophilic water molecule (Wat1), which in turn is activated by the His_{438} imidazole ring (see Scheme 1). The structure of acyl was generated by model building using the X-ray structure of the BuChE enzyme complexed with butyrate (BTY) as a template followed by geometry optimization at the B3LYP/6-31G* level. In the optimized structure, the reactive water molecule is well-poised for catalysis with BTY C1···O Wat1 and Wat1 O···Nϵ His_{438} distances of 3.11 and 2.98 Å, respectively (see Scheme 1 for atom numbering). From acyl, a transition structure (TS1) for the nucleophilic attack of Wat1 toward the ester group with simultaneous Wat1 → His_{438} proton transfer was located on the B3LYP/6-31G* PES. The forming C−O bond at TS1 is quite advanced (1.61 Å), while the proton being transferred is equally bound between the His_{438} Nϵ (N−H = 1.26 Å) and Wat1 O (O−H = 1.26 Å) atoms. Inspection of the transition vector for TS1 confirms that this transition structure corresponds to a *concerted* mechanism for proton transfer and nucleophilic attack (we found that an intermediate structure after the Wat1 → His_{438} proton transfer, which would be relevant for a *stepwise* mechanism, is not a stable minimum on the B3LYP/6-31G* PES). TS1 leads to a tetrahedral intermediate (int) in which the BTY O2 atom interacts closely with the three NH groups of the Gly_{116}, Gl_{117}, and Ala_{199} residues and the BTY O1 atom is hydrogen-bonded to the doubly protonated imidazole ring of His_{438} (see Table 2).

The second step of the hydrolysis process takes place through a TS (TS2) for the rupture of the tetrahedral intermediate with simultaneous proton transfer from His_{438} to the leaving Oγ atom of Ser_{198}. The transition vector of TS2 is dominated by the elongation of the breaking BTY C1···Oγ Ser_{198} bond (1.81 Å) and by proton transfer from His_{438} to Ser_{198} (His_{438} Nϵ···H and Ser_{198} Oγ···H distances

Table 2: Important Interatomic Distances (Å) in the B3LYP/6-31G*-Optimized Structures for the Deacylation of the Butyrate−BuChE Complex

structure	rmsd[a]	Ser_{198} Oγ··· C1 BTY	Ser_{198} Oγ··· Nϵ His_{438}	BTY O1··· Nϵ His_{438}[b]	Glu_{325} Oϵ··· Nδ His_{438}	BTY O1··· Oϵ Glu_{197}[b]	BTY O2··· N Gly_{116}	BTY O2··· N Gly_{117}	BTY O2··· N Ala_{199}
acyl	0.58	1.33	3.07	2.98	2.70	6.27	2.87	4.02	2.80
TS1	0.50	1.42	3.10	2.53	2.74	4.81	2.72	2.90	3.07
int	0.28	1.46	3.01	2.71	2.66	3.95	2.87	3.06	2.78
TS2	0.22	1.81	2.48	3.18	2.59	5.05	2.85	3.04	2.80
prodA	0.26	2.39	2.72	3.16	2.63	4.82	2.71	3.20	2.94
TS3	0.24	2.50	2.74	3.08	2.62	4.62	2.70	3.13	2.98
prodB	1.54	3.11	2.83	3.53	2.67	4.98	2.68	2.87	3.28
X-ray		*2.16*	*2.79*	*3.44*	*2.68*	*5.12*	*2.69*	*3.18*	*2.85*

[a] rmsd of selected QM atoms with respect to the X-ray structure. [b] Note that the BTY O1 and Wat1 O labels refer to the same atom.

Table 3: Relative Energy Components and Free-Energy Corrections (in kcal/mol) of the "Small QM Models" Involved in the Deacylation Process of BuChE[a]

structure	B3LYP/6-311+G** + ZPVE[b]	G_{MM-PB}[c]	E_{MM}[d]	E_{elec}[e]	E_{vdW}[e]	$E_{internal}$[e]	ΔG[f]
acyl	0.0	0.0	0.0	0.0	0.0	0.0	0.0
TS1	4.8	11.0 (0.5)	9.5 (0.6)	8.3 (1.0)	2.2 (0.5)	−1.0 (0.2)	15.8
int	1.3	5.4 (0.6)	5.4 (0.7)	9.5 (1.4)	1.1 (0.8)	−5.2 (0.2)	6.7
TS2	9.3	0.0 (0.5)	−0.2 (0.6)	3.8 (1.1)	0.7 (0.7))	−4.8 (0.2)	9.3
prodA	9.7	−2.4 (0.6)	−5.2 (0.8)	−2.6 (1.3)	1.5 (0.7)	−4.1 (0.2)	7.3
prodB	−14.0	20.1 (0.6)	28.0 (0.7)	28.6 (1.3)	2.9 (0.8)	−3.6 (0.2)	6.1

[a] The MM−PB energy terms correspond to average values derived from 100 snapshots extracted during the last 500 ps of the BCHE−BTY MD−LES simulation and postprocessed according to the MM−PB computational scheme. The standard error of the mean values are given in parentheses. All values are in kcal/mol. [b] From single-point calculations on the small QM models, including the approximate ZPVE correction (see the text for details). [c] Free-energy correction to the QM energies obtained from MM−PB calculations: $G_{MM-PB} = E_{MM} + \Delta\Delta G_{solv}$. [d] MM correction to the QM energies. [e] Electrostatic, van der Waals, and internal (bond-angle-torsional) energy components of the MM energy correction. [f] Approximate free energy of the small QM models in the enzyme: $\Delta G \approx \Delta E_{B3LYP/6-311+G**} + G_{MM-PB}$.

of 1.28 and 1.24 Å, respectively). From TS2, a product complex (prodA) is formed that corresponds to a noncovalent complex between a butyric acid molecule and the enzymatic cluster model. According to our QM calculations, the neutral carboxyl group of the butyric acid in the prodA structure can transfer its proton easily to the carboxylate group of the nearby Glu_{197} residue with the assistance of a bridging water molecule (Wat2) by passing through a low-energy transition structure (TS3). As a consequence, a second product complex (prodB) was obtained on the PES in which the Glu_{197} carboxylate is neutralized, whereas the carboxylate group of the leaving butyrate molecule is retained within the "oxy-anion" hole.

Structure and Energetics of the QM Critical Points. Our QM model of the BuChE active site includes the two main structural components that are commonly thought to be crucial for catalysis: the catalytic triad of residues and the "oxy-anion" hole. There has been some controversy in the literature about the role of the third residue in the catalytic triad, Glu_{325}, in BuChE. In our case, the carboxylate group of Glu_{325} stabilizes the imidazol/imidazolium ring of His_{438} along the reaction profile through a Glu_{325} $COO^{-}\cdots HN\delta$ His_{438} hydrogen bond with a heavy-atom distance of 2.70−2.60 Å (see Table 2). The closest contact occurs at TS2 (2.59 Å), suggesting that the stabilizing role of Glu_{325} is particularly important for the rupture of the C−O bond. This short distance could be interpreted as indicative of a short and strong hydrogen bond, although previous QM/MM calculations on AChE have shown that there is a notable energy barrier for proton transfer from the catalytic His to Glu residues (*26*). To further examine this point, we optimized a QM model of the tetrahedral intermediate having a Glu_{325} $COOH\cdots\delta N$ His_{438} hydrogen bond. The resulting structure was 14 kcal/mol less stable than int at the B3LYP/6-311+G**//B3LYP/6-31G* level of theory, and therefore, neutralization of the $Glu_{325}\cdots His_{438}$ salt bridge during catalysis would be unlikely. This result contrasts with recent QM/MM calculations on the hydrolysis reaction of cocaine catalyzed by BuChE in which a neutral $Glu_{325}\cdots His_{438}$ pair is observed (*29*). This discrepancy could be in part due to the different level of theory employed for geometry optimizations (B3LYP/6-31G* in this work and HF/3-21G in the BuChE−cocaine calculations). In the QM/MM calculations, the neutral state of the $Glu_{325}\cdots His_{438}$ pair might be stabilized by the presence of a negative charge on the buried Glu_{441} residue (this residue interacts through a water molecule with the Glu_{325} carboxylate group). In our MD simulations and MM−PB calculations (see below), Glu_{441} is neutralized as indicated by our previous pK_a calculations (*44*).

Another remarkable feature of the catalytic process as described by the QM calculations is that the three-pronged "oxy-anion" hole formed by the NH groups of Ala_{199}, Gly_{116}, and Gly_{117} is perfectly adapted for binding the negatively charged BTY O2 atom of the TS1, int, and TS2 structures, because each structure has three NH···O hydrogen-bond contacts with heavy-atom distances of 2.7−3.0 Å (see Table 2). In the other QM structures (acyl, prodA, TS3, and prodB), two of the NH···O contacts have N···O distances of about 2.8 Å, whereas the third contact has an N···O distance longer than 3.2 Å.

At the B3LYP/6-311+G**//B3LYP/6-31G* level of theory, the rate-determining step corresponds to the rupture of the tetrahedral intermediate via TS2 with an energy barrier of 19.3 kcal/mol with respect to the acyl−enzyme structure (15.9 kcal/mol including the B3LYP/6-31G* ZPVE correction). The tetrahedral intermediate int is only 1.2 kcal/mol more stable than TS1, which has a ΔE value of 8.1 kcal/mol. However, inclusion of the ZPVE correction makes int a transient structure because it becomes less stable than TS1 by 1.1 kcal/mol. Similarly, the B3LYP/6-311+G**//B3LYP/6-31G* energy of the first product complex, prodA, is only 0.9 kcal/mol lower than that of TS3, which is the transition structure for prodA to donate its acidic hydrogen to the Glu_{197} carboxylic group. When the ZPVE correction is added to the electronic energies, prodA is less stable than TS3, becoming a transient species, such as the tetrahedral intermediate int. The final product complex, prodB, is 14.5 kcal/mol more stable than the initial acyl−enzyme complex.

To check the sensitivity of the energy profile to the polarity of the environment, we performed single-point SCRF energy calculations on the gas-phase QM geometries using three different values for the dielectric constant of the surrounding continuum ($\epsilon = 80$, 20, and 4). From the relative solvation energies ($\Delta\Delta G_{solv}$) included in Table 1, we see that all of the dielectrics tend to stabilize preferentially the tetrahedral intermediate int and the rate-determining TS2 structure by 3−4 kcal/mol and to favor the product complex prodA with respect to prodB. Nevertheless, these results should be treated with caution because protein−solvent environments are not homogeneous media characterized by a single dielectric constant.

The Nature of the BTY C1···Oγ Ser_{198} Interaction. Our QM calculations help to clarify the rather enigmatic character of the tetrahedral adduct observed in the X-ray structure of

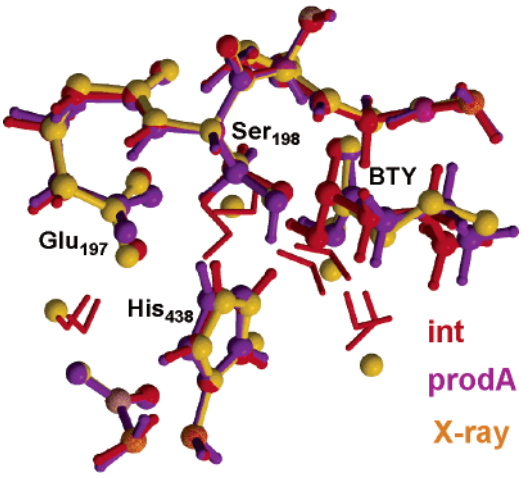

FIGURE 1: Superposition of the QM cluster models (int and prodA) onto the X-ray structure.

BuChE (*10*). The rmsd values between the protein heavy atoms in the int QM-optimized model and the X-ray structure and between the same atoms in the prodA model and the X-ray structure are low and have quite similar values of 0.22 and 0.26 Å, respectively. However, inspection of the interatomic distances collected in Table 2 enables us to discriminate between int and prodA. Thus, the BTY C1···Oγ Ser$_{198}$ distance at prodA, 2.39 Å, compares reasonably well with the X-ray value of 2.16 Å, whereas the int structure displays a typical C−O bond distance of 1.46 Å. Curiously, the C1 sp^2 atom of the butyryl moiety at prodA retains a slight tetrahedral character (the O1−C1−O2−C2 dihedral angle is 172.9°), although it is less accentuated than those in the optimized int model (124.0°) and in the X-ray structure (138.8 °). Additionally, we also compared the His$_{438}$ Cδ2···Nϵ2 His$_{438}$···Oγ Ser$_{198}$ angle, which is 168°, 175°, and 170° at the prodA, int, and X-ray structures, respectively. Concerning the three important N···O2 BTY contacts defining the "oxy-anion" hole interactions, the X-ray structure has a closer match to the optimized prodA structure (see Table 2). This is also shown in Figure 1, in which the prodA, int, and X-ray structures are superposed onto each other. Overall, we conclude that prodA should be considered the best QM model for the structure of the butyryl moiety determined crystallographically (*10*).

To further characterize the unusual C··O nonbonding interaction, we used the tools provided by the theory of atoms in molecules (*34*), which is able to identify and classify atomic interactions in terms of the topological properties of the electron density [$\rho(r)$] and the Laplacian of the electron density [$\nabla^2\rho(r)$]. The evolution of the BTY C1···Oγ Ser$_{198}$ interaction along the reaction profile is reflected in changes in the properties of the BCP between the C1 and Oγ nuclei. During the first step of the reaction, the BTY C1−Oγ Ser$_{198}$ bond is weakened because the $\rho(r_c)$ and energy density [$H(r_c)$] values at the BCP decrease but its polar and covalent character is maintained as revealed by the negative sign and large magnitude of $\nabla^2\rho(r_c)$ (see Table S1 in the Supporting Information). A qualitative change in the BTY C1−Oγ Ser$_{198}$ interaction occurs during the second step: the covalent C−O bond is transformed into a C(sp^2) ← :O interaction that has BCP properties typical of donor → acceptor interactions between closed-shell systems, such as found in hydrogen bonds and van der Waals molecules (a small $\rho(r_c)$ value, a small and positive $\nabla^2\rho(r_c)$, etc.). It must be noted that the existence of the BTY C1···Oγ Ser$_{198}$ BCP in prodA (and TS3) demonstrates that the butyric carboxyl and the Ser$_{198}$ hydroxyl groups establish a stabilizing contact (*49*). In contrast, the corresponding BCP is not found in the electron density of the prodB structure, in which the carboxylate group of the butyrate moiety is 3.11 Å away from the Ser$_{198}$ hydroxyl group.

For comparative purposes, we also investigated the binding energy and equilibrium distance of the C(sp^2) ← :O(sp^3) interaction in a small model system, a $CH_3COOH\cdots H_2O$ dimer, which is relevant to the noncovalent complex between the butyric acid and the Ser$_{198}$ hydroxyl group at the prodA structure. Both the B3LYP density functional and the ab initio MP2 methods were used to carry out constrained geometry optimizations of the small complex by forcing the water oxygen atom to lie in a plane perpendicular to the carboxyl group of the acetic acid molecule (see Figure S2 in the Supporting Information). The equilibrium C(acetic acid)···O(water) distances are in the 2.85−3.19 Å range depending upon the level of theory (MP2 tends to give shorter distances than B3LYP). These distances are more than 0.5 Å longer than that found in the prodA model (2.39 Å) and show that substituent and environmental effects could reinforce the C(sp^2)···O(sp^3) interaction seen in prodA. On the other hand, the BSSE-corrected counterpoise binding energy amounts to 1.6 kcal/mol at the B3LYP/6-311+G(2d,2p) and CCSD(T)/6-311+G(2d,2p)//MP2/6-311+G(2d,2p) levels of theory. This binding energy value for the $CH_3COOH\cdots H_2O$ dimer, which is similar to those of weak van der Waals complexes, suggests that the similar C(sp^2) ← :O(sp^3) interaction seen in the QM prodA model could have a weakly attractive character.

When the structural and electronic analyses of the BuChE QM models are taken together, along with the test calculations on the water−acetic acid dimer, they support the designation of the butyrate group determined crystallographically as a noncovalent complex formed between a butyric acid molecule and the enzyme. In this complex, the Ser$_{198}$ hydroxyl and the butyric carboxyl groups establish a donor−acceptor interaction that explains the unusually short C···O distance observed experimentally. Nevertheless, the QM calculations also indicate that prodA would be short-lived and that the much more stable prodB complex lacks the C··O interaction. Hence, energy calculations that take into account the protein and solvent environment are needed to determine whether the presence of a butyric fragment bound to the active site of BuChE is thermodynamically favorable.

Protein and Solvent Effects: Relative Energies of the Small QM Models. As described in the Materials and Methods, protein and solvent effects were included in our computational analyses of the deacylation reaction of BuChE by combining the average MM−PB free energies, evaluated for a series of MD snapshots of the solvated BuChE enzyme, with the B3LYP/6-311+G** energies of the small QM models representing the reactive region. The atoms in the small QM models are a subset of those in the acyl, TS1, int, TS2, prodA, and prodB structures and comprise the butyrate moiety, the "oxy-anion hole" residues, Glu$_{197}$, Ser$_{198}$, His$_{438}$, and Glu$_{325}$, and the Wat1 molecule. Their relative gas-phase energies, which were obtained through single-point B3LYP/6-311+G** calculations, are 0.0, 7.1, 1.3, 12.6, 10.1, and

−13.5 kcal/mol energy, respectively. We also derived an *approximate* ZPVE correction for the small QM model systems by normal-mode analysis of a Hessian submatrix extracted from the full B3LYP/6-31G* Hessian matrix of the large QM models. The addition of the ZPVE correction gives the following relative energies: 0.0, 4.8, 1.3, 9.3, 9.7, −14.0 kcal/mol for acyl, TS1, int, TS2, prodA, and prodB, respectively. In this case, prodA turns out to be unstable.

When the relative energies of the small QM models are compared with those of the large cluster models, it turns out that the energy barriers for the deacylation process are significantly lower for the small QM models. Thus, for example, the B3LYP/6-311+G** energy barrier associated with the TS2 structure decreases from 19.4 to only 12.6 kcal/mol when the coordinates of the three nonreactive water molecules, the Ser_{224} side chain, and the Val_{321}−Asn_{322} peptide linkage are removed. This suggests that microsolvation effects, mainly exerted by the water molecules in the large cluster structures, have an anticatalytic effect on the energy profile and that the essential catalytic machinery is provided by the three-pronged "oxy-anion hole" and the Ser_{198}−His_{438}−Glu_{325} triad of residues. Nevertheless, the long-range interactions between the reactive region and the surrounding BuChE system must be taken into account for a more complete view of the enzymatic process.

Stability of the MD−LES Trajectories. We carried out MD simulations using the LES technique to sample the most likely enzyme and solvent conformations in the presence of MM representations of three small QM models embedded within the BuChE gorge (the "LES copies"). During the MD simulations, the geometry of the LES copies was kept frozen, whereas the rest of the enzymatic system and water molecules were allowed to move. As mentioned above, four different MD−LES simulations were computed: BCHE−BTY (the gorge cavity is filled with water molecules), BCHE−BTY−Na (a sodium cation is also present), BCHE−BTY−GOL (a GOL molecule is bound between the Glu_{197} carboxylate and the BTY moiety), and BCHE−BTY−CHO (a CHO molecule is bound to the intermediate site). Figure 2 shows schematic representations of the relevant hydrogen-bond contacts observed in the active site and characteristic snapshots extracted from the MD−LES trajectories.

An analysis of the rmsd values of the dynamical structures from the four MD−LES simulations with respect to the initial crystal structure indicates that the trajectories evolved to an equilibrated state. The average rmsd values (1.75−1.81 Å) are quite similar to those observed in simulations of the native form of the BuChE enzyme (*44*). Similarly, in the four simulations, the accessibilities of the butyrate moiety, the cation−π site, and the acyl-binding pocket (collected in Table S3 in the Supporting Information) are similar to those that we observed previously (*44*).

The segregation of the rmsd values into distinct motifs shows that the largest deviations among the four MD−LES trajectories arise in the BuChE gorge region, and occur mainly in residues of various long loops, such as the Ω loop (Cys_{65}−Cys_{92}) and the acyl loop (Pro_{281}−Asp_{301}) and also in embedded short α-helical segments (see Table S2 in the Supporting Information). For example, the average rmsd values of the acyl-loop residues have values of 3.17 ± 0.18, 3.10 ± 0.11, 2.98 ± 0.18, and 2.78 ± 0.26 Å for the BCHE−BTY, BCHE−BTY−Na, BCHE−BTY−GOL, and BCHE−BTY−CHO protein configurations, respectively. These observations indicate that the active-site gorge is slightly rigidified in the presence of small molecules, although we confirmed visually that the most important conformational differences arise in the side chains of solvent-exposed residues in the Ω and acyl loops.

The BCHE−BTY Configuration. In our previous work on the structure and dynamics of the native form of the BuChE enzyme (*44*), we found that the water molecules populating the active-site region established organized networks of hydrogen bonds interconnecting polar protein groups. Most notably, the Glu_{197} carboxylate group played a central role in the water-mediated network of hydrogen bonds by establishing long-lived associations with the buried Glu_{441} and Ser_{224} side chains, the His_{438} Nϵ and Ser_{198} Oγ atoms of the catalytic triad, and the amide NH groups at the "oxy-anion hole". The water molecules with large residence times (>3 ns) were those that constituted the one-water bridges interconnecting the catalytic groups. Two of the water molecules with reduced mobility connecting the "oxy-anion" hole and the Ser_{198} hydroxyl group are replaced by the BTY moiety in the BCHE−BTY configuration, but other important structural water bridges remain perfectly stable as shown schematically in Figure 2a, in which average distances between heavy atoms and the percentage of occurrence data are also summarized. Of particular importance are the Glu_{197} COO···(H_2O)···HO BTY and Glu_{197} COO···(H_2O)···Nϵ His_{438} bridges with 70 and 77% occurrence, respectively, because these water molecules closely solvate the groups undergoing a chemical reaction during the deacylation process. Moreover, the BCHE−BTY MD−LES simulation, in which the acyl, int, and prodA small QM models are simultaneously present in the MM force field as different "LES copies", shows that these water bridges are structurally and dynamically conserved along the reaction coordinate.

As described in the Materials and Methods, all of the reactive MM models (acyl, TS1, int, etc.) built from their parent small QM models were embedded within the structures of 100 snapshots extracted from the BCHE−BTY MD−LES trajectory. For each reactive MM model, the structures were relaxed by means of MM energy minimizations, in which only the solvent molecules and the residues adjacent to the reactive MM model were allowed to move. These minimizations maintained the identity and properties of the important hydrogen-bond interactions and water bridges that interconnect the catalytic residues and BTY moiety. Subsequently, we carried out the MM−PB energy calculations on the whole enzymatic system and the reactive MM models to estimate the average free-energy corrections that take into account the environmental effects along the deacylation reaction coordinate. The resulting average values of the MM−PB free energies and MM energy components are shown in Table 3.

The G_{MM-PB} values in Table 3 are the MM−PB free-energy corrections to the B3LYP/6-311+G** + ZPVE energies of the small QM models. When we go from the transition structure for water activation and nucleophilic attack, TS1, to the product complex, prodA, the relative G_{MM-PB} values decrease monotonically from 11.0 to −2.4 kcal/mol. As a result, the approximate free-energy profile in the enzyme changes with respect to that in the gas phase because the rate-determining barrier now corresponds to the

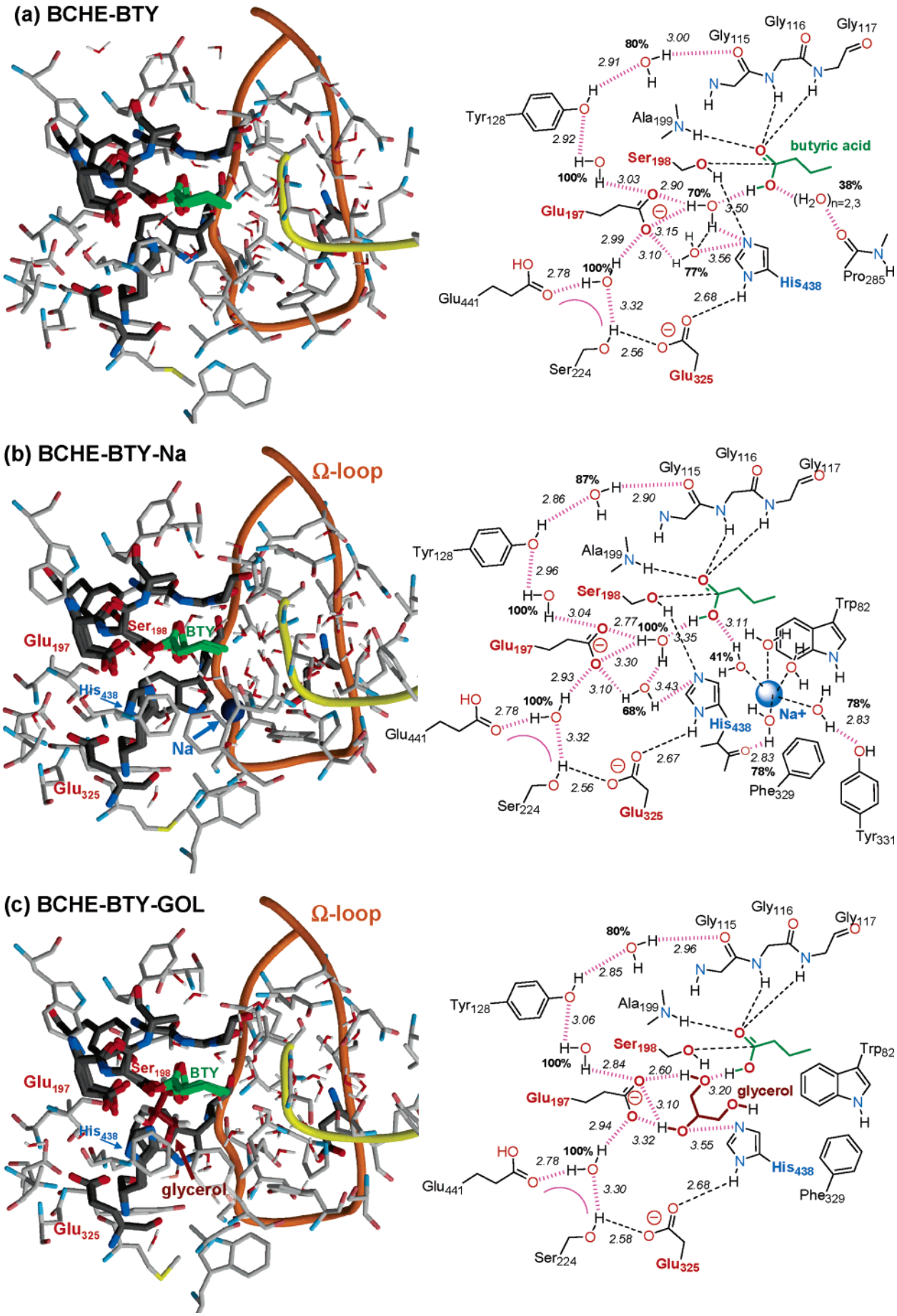
(a) BCHE-BTY
butyric acid
(b) BCHE-BTY-Na
Ω-loop
BTY
Na
(c) BCHE-BTY-GOL
Ω-loop
BTY
glycerol

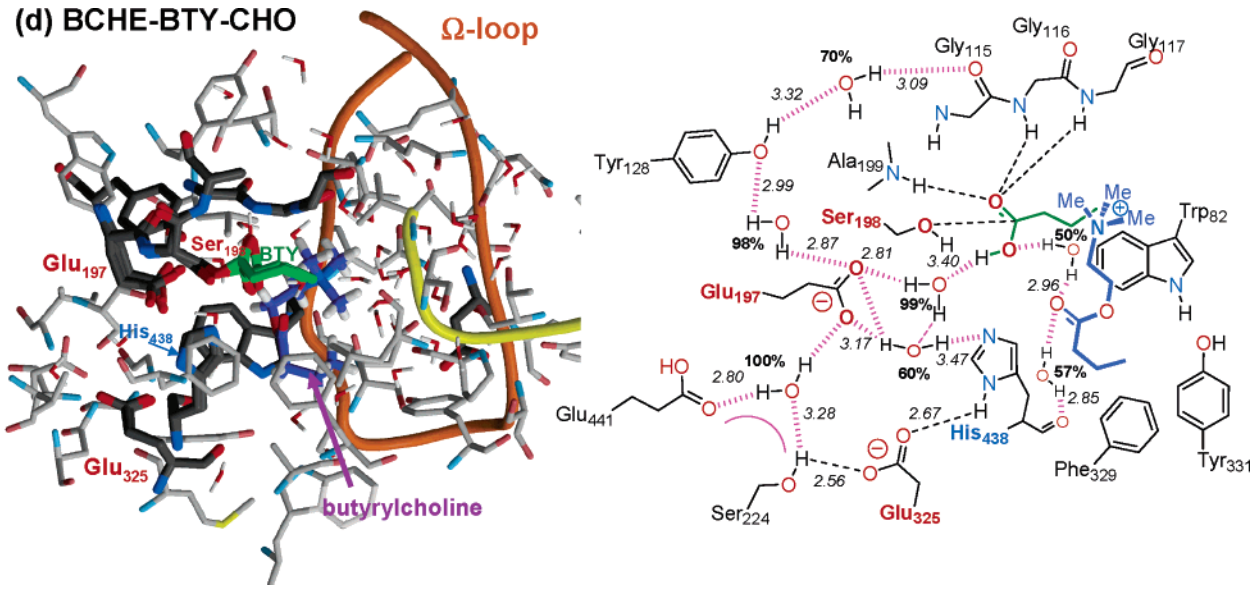

FIGURE 2: Schematic representation of the main hydrogen-bond contacts and water bridges observed in the BuChE active site (a−d) along the four MD−LES trajectories computed for the BuChE−butyrate complex. The snapshots of the active sites extracted from each simulation were produced with Molscript and Raster3D.

transition structure (TS1) for the formation of the tetrahedral intermediate (int). The average G_{MM-PB} values combined with the density functional theory (DFT) energies lead to an energy barrier of ~16 kcal/mol, which seems quite reasonable (see Table 3). The tetrahedral intermediate, whose approximate free energy in the enzyme is ~9 and ~3 kcal/mol below those of TS1 and TS2, respectively, becomes a stable structure along the reaction profile. On the other hand, the relative stability of the product complexes, prodA and prodB, is very sensitive to protein and solvent effects. Thus, in the gas phase, the butyric moiety at prodA readily transfers a hydrogen atom to the carboxylate group of the Glu_{197} side chain to give the prodB complex, in which the negatively charged butyrate is tightly bound to the "oxy-anion" hole. In contrast, in the enzyme, prodA and prodB have a similar free energy because the greater intrinsic stability of prodB is largely compensated by the electrostatic interactions of the reactive MM model with the rest of the protein. As a result, our calculations predict that prodA would be less stable than prodB in the protein by only ~1 kcal/mol.

Inspection of the free-energy components in Table 3 reveals that the intraprotein electrostatic energy (E_{elec}) dominates the G_{MM-PB} terms. The positive sign of the G_{PB-MM} and/or E_{elec} terms corresponding to the TS1 and int structures suggests that the rest of the BuChE enzyme not included in the small QM models has actually an anticatalytic effect during the formation of the tetrahedral intermediate. This was not entirely unexpected given that the B3LYP/6-311+G** energy of the gas-phase small QM models is very low because of the stabilization of the TS1 and int structures by the short hydrogen-bond interactions of the BTY O2 atom with the "oxy-anion" hole. These O···H−N interactions, in turn, polarize the amide backbone groups of Gly_{116}, Gly_{117}, and Ala_{199}. However, this polarization effect, which is taken into account by the HF/6-31+G* RESP atomic charges, implies less favorable electrostatic intraprotein interactions and explains the positive values of the G_{MM-PB} energies. Similarly, the large stabilization of prodA with respect to prodB can be traced to the placement of the negative charge within the "oxy-anion" hole at prodB, which is electrostatically disfavored when the surrounding protein is included in the MM calculations. On the other hand, other energy contributions such as E_{vdW} and E_{int}, which have a lower impact on G_{MM-PB} than that of E_{elec}, can also discriminate among the different QM models. For example, the internal energy, which tends to destabilize the acyl−enzyme structure, is dominated by the bending energy terms involving the Tyr_{114}−Gly_{115}, Gly_{117}−Phe_{118}, and Ala_{199}−Gly_{200} peptide linkages. These bond angles change slightly as the geometry of the "oxy-anion" hole moiety adapts to the presence of the NH···O(BTY) contacts.

The BCHE−BTY−Na Configuration: Influence of the Na^+ Cation. Our previous MD simulations of the native form of the BuChE enzyme (*44*) indicate that the presence of one Na^+ ion in the gorge cavity stabilizes the hydrogen-bond network interconnecting the catalytic triad of residues and the important water bridges. To find out if a Na^+ ion could have a similar effect in the presence of the BTY fragment at different stages of the deacylation process, we examined the BCHE−BTY−Na configuration in which a Na^+ cation is bound to the BuChE cation−π site.

During the BCHE−BTY−Na MD−LES simulation, the Na^+ ion showed a stable first solvation shell comprising 5−6 water molecules and was located close to the indole group of Trp_{82} (the cation−π binding site), the side chain of Tyr_{331}, the BTY carboxylic group, and the backbone carbonyl group of His_{438} (see Figure 2b). In terms of other important hydrogen-bond interactions and water bridges, the structural results were similar to those of the BCHE−BTY trajectory. However, it is interesting to note that there is a higher abundance (100%) for the one-water bridge linking the Glu_{197} carboxylate and the BTY−carboxyl groups. Thus, the presence of the hydrated Na^+ cation at the cation−π site seems to reduce the water mobility around the reactive BTY fragment.

The calculated free-energy profile for the BCHE−BTY−Na configuration (see Figure 3) indicates that, with respect to the BCHE−BTY configuration, the presence of the Na^+

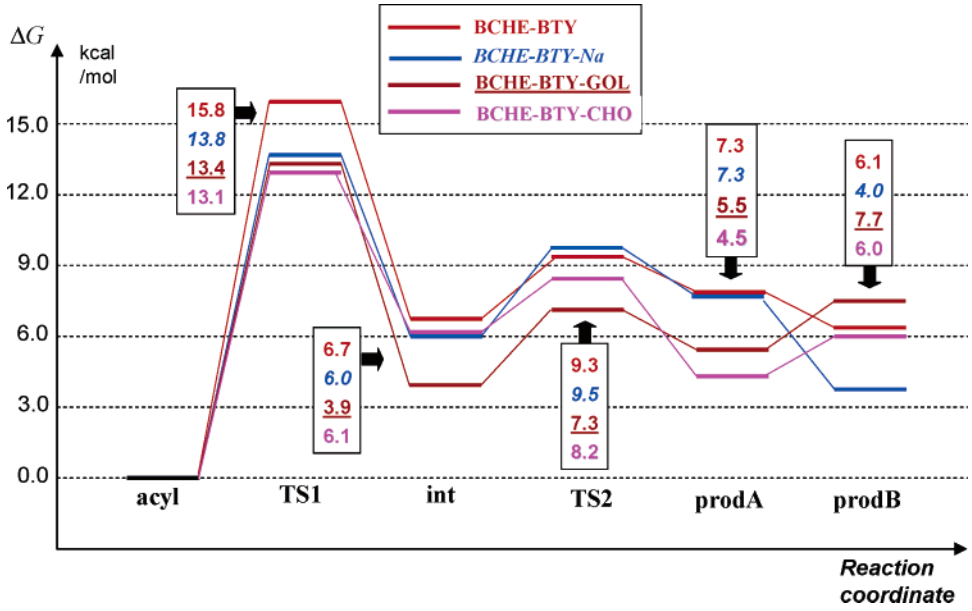

FIGURE 3: Schematic free energy (ΔG) profiles in the enzyme. The ΔG values combine the relative QM energies and free-energy corrections (G_{MM-PB}) of the "small QM models" involved in the deacylation process of BuChE. The G_{MM-PB} energy terms correspond to average values derived from 100 snapshots extracted during the last 500 ps of the BCHE−BTY, BCHE−BTY−Na, BCHE−BTY−GOL, and BCHE−BTY−CHO MD−LES simulations. All values are in kcal/mol.

ion does not alter significantly the relative energies of the small QM models in the enzyme, except for the TS1 and prodB structures, which tend to be stabilized (their corresponding ΔG values are ∼2 kcal/mol lower than in the absence of Na^+). In fact, the energetic influence of the Na^+ cation is partially exerted through the vdW energy terms, which are largely controlled by the differential solvent rearrangement around the BTY and the catalytic triad of residues (see data in Table S4 in the Supporting Information). Overall, our simulations suggest that the Na^+ ion has only modest kinetic and thermodynamic effects in consonance with the experimental evidence (*16*) that, in the presence of NaCl, the rate of deacylation for native BuChE is relatively unaltered (although it is conceivable that BuChE would retain a positive small cation even in the absence of external NaCl).

Influence of One Glycerol Molecule: Why Is BTY Bound to the BuChE Active Site in the X-ray Structure? X-ray structures of both "native" and soman-aged BChE have a GOL molecule (used as cryoprotectant) placed between the Glu_{197} carboxylate and the Trp_{82} indole groups (i.e., the cation−π site) (*10*). Because GOL has no physiological role with BuChE, its presence in the active-site gorge confirms the broad specificity of the cation−π site. The question also arises about the influence of GOL or similar neutral molecules on the deacylation process, especially on the relative stability of prodA with respect to prodB. To further investigate this point, we carried out the BCHE−BTY−GOL MD−LES simulation of the BChE−butyrate complex in the presence of GOL. During the BCHE−BTY−GOL simulation, the GOL molecule remained bound to the Glu_{197} carboxylate and butyric carboxylic groups through very stable OH···O interactions (see Figure 2c). In this way, the GOL molecule replaces the two water molecules that constitute the Glu_{197}···His_{438} and Glu_{197}··BTY water bridges in the BCHE−BTY and BCHE-BTY−Na configurations and provides a less flexible "first solvation shell" around the reactive groups.

The energetic analyses show that the GOL molecule modifies slightly the energy profile for the deacylation process by stabilizing the TS1, int, TS2, and prodA structures by ∼2 kcal/mol. The rate-determining energy barrier is now 13.4 kcal/mol. The stabilization effect of GOL stems from a mixture of electrostatic and vdW interactions and is perfectly consistent along the reaction profile. Most interestingly, the prodB complex turns out to be destabilized by the nearby GOL molecule so that prodA is ∼2 kcal/mol below prodB in terms of the estimated ΔG values (see Figure 3).

On one hand, the QM calculations on the large cluster model prodA give molecular geometries and electronic properties that allow us to understand the "long BTY C1····Oγ-Ser_{198} bond" observed experimentally in terms of a donor−acceptor noncovalent interaction. On the other hand, the MD−LES and MM−PB calculations carried out on the BCHE−BTY−GOL configuration predict that the prodA product complex is stabilized by enzyme electrostatic effects and the occupation of the cation−π site by GOL. We note, however, that our computational analyses do not provide a definitive explanation for the presence of butyric acid in the crystal state because the predicted ΔG of prodA in the enzyme is still positive (+6 kcal/mol) with respect to the acyl−enzyme structure. In part, this may be due to limitations in our computational approach, some of which are (i) higher levels of theory that may be required for accurate prediction of the ΔE_{elec} energies, (ii) uncertainties in the MM representation of the reactive small QM models, (iii) several geometrical constraints that were imposed in the MD−LES and MM−PB calculations, and (iv) the MD−LES sampling of the free-energy components that has a significant statistical imprecision.

Influence of One Butyrylcholine Molecule Bound to the Cation−π Site. Human BuChE is activated by low concentrations of substrate molecules. This kinetic effect is thought to be a consequence of a three-step mechanism for substrate binding that precedes the formation of the acyl−enzyme

intermediate (*4*). In the first BuChE−substrate complex (ES1), the Asp_{70} residue, strategically located at the mouth of the aromatic gorge, would serve to stabilize and orient the substrate. To form the second complex (ES2), the substrate molecule would slide down the gorge so that its choline head has a cation−π interaction with the Trp_{82} indole ring. Finally, ES2 should rearrange into a productive complex ES3, in which the substrate butyryl group is placed at the bottom of the active-site cavity in a position suitable for hydrolysis. In this scenario, substrate activation would occur when ES2 is formed between a substrate molecule and BuChE is in its acyl−enzyme form.

To obtain insight into the influence of a nonreactive CHO molecule, we carried out a 1 ns MD−LES simulation of the ternary complex BChE−butyrate−CHO. The initial positioning of CHO was selected using the X-ray structure of the BuChE−soman−butyrylthiocholine complex as a template (*10*). In the X-ray structure, the positively charged choline head points toward the indole group of Trp_{82} occupying the cation−π site. Along the BCHE−BTY−CHO simulation (see Figure 2d), the orientation of the CHO molecule within the active-site cavity changes so that its choline head is more oriented toward the gorge mouth (although it remains close to the cation−π site with an average distance between the CHO N atom and the center of mass of the Trp_{82} side chain of 5.1 ± 0.7 Å) and its carbonylic O atom establishes quite stable water bridges (∼50%) with the hydroxyl BTY group and the His_{438} carbonyl group. Likewise, in the presence of the gorge Na^+ cation, the Glu_{197}···BTY water bridge is perfectly stable (100%) when the CHO molecule is bound to the cation−π site. The average G_{MM-PB} corrections in the BCHE−BTY−CHO configuration show that TS1 is stabilized by ∼3 or ∼1 kcal/mol with respect to the BCHE−BTY and BCHE−BTY−Na simulations (see Figure 3), respectively, through an interplay of electrostatic and vdW influences.

Concerning the relative stability of the product complexes, prodA ($\Delta G \sim 5$ kcal/mol) is more stable than prodB in the presence of CHO. Because the Na^+ cation does not stabilize prodA, we conclude that the CHO effect is not due to its positive charge but to the occupation of the cation−π site. Moreover, these results and those observed for the BCHE−BTY−GOL state indicate that the stabilization of prodA depends little upon the actual structure of the molecule bound to the cation−π site. It is also interesting to note that the stabilization of prodA could have interesting mechanistic consequences. Because the leaving butyric molecule would be neutral in the presence of an incoming CHO molecule, its diffusion away through the acyl-loop *back door* should not be retarded by electrostatic pulling forces exerted by the positively charged CHO choline head (a channel leading to the acyl-loop back door is formed in the thin acyl-pocket wall between the Leu_{285} side chain and the Trp_{231} Cβ atom) (*44*).

Comparison with Previous Calculations on the Deacylation Reaction of AChE. It is interesting to compare our results with those of Vagedes et al. for the deacylation reaction of the AChE enzyme (*25*). These authors studied only the formation of a tetrahedral intermediate and considered both stepwise (Wat → His_{438} proton transfer and nucleophilic attack of a hydroxide moiety to the ester group) and concerted (simultaneous proton transfer and nucleophilic attack) reaction mechanisms. Different sets of EVB parameters were used for the simulations of each pathway. The EVB/FEP calculations showed that the concerted and stepwise pathways were nearly isoenergetic. In this work, we investigated only the concerted route for the formation of the nucleophilic intermediate because this was the only one that we found to exist from our B3LYP/6-31G* cluster-model geometry optimizations. Nevertheless, we cannot completely exclude the possibility of a stepwise route if higher levels of the QM theory were to be used or larger cluster models were to be considered. The EVB/FEP calculations revealed that the rate enhancement exerted by AChE is very high (by a factor of $\sim 10^8-10^9$), with the reported energy barriers in the enzyme being between 15.0 and 18.0 kcal/mol depending upon the EVB parameter set. Although we do not compute the catalytic effect of the BuChE enzyme, the magnitude of the free-energy barriers in Figure 3 (13−15 kcal/mol) is similar to those for AChE. Interestingly, Vagedes et al. found that the presence of a choline molecule in the cation−π binding pocket of AChE lowers the activation barrier by 1.2 kcal/mol. This result agrees with the kinetic effects observed in the BuChE enzyme when the cation−π site is occupied. On the other hand, Vagedes et al. predict that the neutral Glu_{197} residue (Glu_{199} in AChE residue numbering) stabilizes the rate-determining TS by around ∼4 kcal/mol according to EVB/FEP estimates and that Glu_{197} should be neutralized in AChE based on Monte Carlo PB calculations of pK_a shifts. In the case of BuChE, however, our previous pK_a calculations indicated that Glu_{197} is unprotonated (*44*).

SUMMARY AND CONCLUSIONS

In this work, we employ QM computational methodologies to characterize a family of cluster models that are relevant to the deacylation reaction in the BuChE enzyme. The analyses of the equilibrium geometries, electronic properties, and energies of the large QM cluster models gave insights into the catalytic mechanism of this important enzyme. The most interesting results and conclusions obtained from our calculations on the cluster models are (a) The QM reaction pathway for the deacylation of the initial acyl−enzyme complex involves a single proton transfer along the His_{438} Nϵ-H····Oγ Ser_{198} hydrogen bond, whereas there is no proton transfer between His_{438} and Glu_{325}. The QM calculations also highlight the crucial catalytic role of the "oxy-anion hole" at the transition states and tetrahedral intermediate, by establishing three N−H···O contacts with heavy-atom distances of 2.7−3.1 Å. (b) On the basis of the electronic properties and equilibrium geometry of the prodA cluster model, the "long BTY C1····Oγ Ser_{198} bond" detected experimentally can be assigned to a noncovalent donor−acceptor interaction between the carbonylic C atom of the butyric acid molecule and the Ser_{198} hydroxylic O atom. (c) In the gas phase, both the tetrahedral intermediate (int) and the product complex (prodA) should be very short-lived species and the hydrolysis of the initial acyl−enzyme structure would proceed through a single-step mechanism leading to the product complex prodB, in which the Glu_{197} carboxylate group is protonated.

The QM cluster models provided reference geometries and atomic charge distributions that were employed to construct the MM representations of the reactive region of the

BuChE−butyrate complex at different stages of the reaction pathway for the deacylation process. These "reactive MM models" allowed us to employ complementary MD−LES and MM−PB methodologies to estimate the energetic effects in various enzymatic configurations. The most important results obtained from the MM−PB calculations are (d) When the free-energy corrections (G_{MM-PB}), which take into account the effects of the fluxional protein and solvent environment interacting with the "reactive MM models", are added to the QM energies of the corresponding small QM models, the rate-determining step is the formation of the tetrahedral intermediate. The latter, in turn, becomes an energetically stable structure, although it would not accumulate during the reaction process. The magnitude of the energy barrier ranges from 13 to 16 kcal/mol depending upon the exact enzymatic configuration. (e) When MD−LES simulations are carried out in the presence of a Na^+ ion or a neutral GOL molecule bound to the cation−π site, we found that both the Na^+ cation and the GOL molecule stabilize the network of hydrogen-bond interactions between the reactive groups and affect the energy profile for the deacylation process by decreasing the energy barrier by ∼2 kcal/mol. (f) Glycerol stabilizes preferentially the product complex formed between a (neutral) butyric acid molecule and the BuChE enzyme instead of the product complex between a (negatively charged) butyrate and BuChE with protonated Glu_{197}. This is in agreement with the crystallographic structure of the BuChE enzyme, in which both a butyric acid molecule and a GOL molecule were detected. (g) The results of the BCHE−BTY−CHO simulation give support to the previous proposal that the deacylation process can occur with the simultaneous binding of a second nonreactive CHO molecule to the cation−π site. The MM−PB energy calculations show that the presence of CHO results in the decrease of the energy barrier by ∼3 kcal/mol with respect to the BCHE−BTY configuration (∼1 kcal/mol with respect to BCHE−BTY−Na). These computational observations are consistent with the assumption that substrate activation exhibited by BuChE arises from the speed up of the deacylation process. (h) The modulation of BuChE activity, exerted by either GOL or CHO bound to the cation−π site, does not involve any significant conformational change (i.e., an allosteric effect) of the gorge residues. Our results point out that the nonreactive molecules (GOL or CHO) belong to the first "solvation shell" surrounding the reactive fragments of the BuChE−butyrate complex and can favor the reaction process by simply modifying the average structure and energetics of this shell.

ACKNOWLEDGMENT

We are grateful to the CEA (France) and CIEMAT (Spain) for generous allocations of computer time. N.D. and D.S. thank all of the members of the LDM for their warm hospitality. The authors thank S. Martí (UJI, Spain) for the coordinates of the chorismate mutase system.

SUPPORTING INFORMATION AVAILABLE

Tables S1−S10, Figures S1−S4, results from validation calculations, and GOL and CHO parameters in a format suitable for the LEaP program (33 pages). This material is available free of charge via the Internet at http://pubs.acs.org.

REFERENCES

1. Doctor, B. P., Taylor, P., Quinn, D. M., and Rotundo, R. L. (1999) *Structure and Function of Cholinesterases and Related Proteins*, Plenum Pub. Corp., London, U.K.
2. Massoulie, J., Bacou, F., Barnad, E., Chatonnet, A., Doctor, B. P., and Quinn, D. M. (1991) *Cholinesterases: Structure, Function, Mechanism, Genetics and Cell Biology*, American Chemical Society, Washington, DC.
3. Silman, I., and Sussman, J. L. (2005) Acetylcholinesterase: "Classical" and "non-classical" functions and pharmacology, *Curr. Opin. Pharmacol. 5*, 293−302.
4. Masson, P., Legrand, P., Bartels, C. F., Froment, M.-T., Schopfer, L. M., and Lockridge, O. (1997) Role of aspartate 70 and tryptophan 82 in binding of succinyldithiocholine to human butyrylcholinesterase, *Biochemistry 36*, 2266−2277.
5. Gorelick, D., Gardner, E., and Xi, Z. (2005) Agents in development for the management of cocaine abuse, *Drugs 64*, 1547−1573.
6. Nigg, H. N., and Knaak, J. B. (2000) Blood cholinesterases as human biomarkers of organophosphorus pesticide exposure, *Rev. Environ. Contam. Toxicol. 163*, 29−111.
7. Geula, C., and Darvesh, S. (2004) Butyrylcholinesterase, cholinergic neurotransmission and the pathology of Alzheimer's disease, *Drugs Today 40*, 711−721.
8. Darvesh, S., Hopkins, D. A., and Geula, C. (2003) Neurobiology of butyrylcholinesterase, *Nat. Rev. Neurosci. 4*, 131−138.
9. Sussman, J. L., Harel, M., Frolow, F., Oefner, C., Goldman, A., Toker, L., and Silman, I. (1991) Atomic structure of acetylcholinesterase from *Torpedo californica*: A prototypic acetylcholine-binding protein, *Science 253*, 872−879.
10. Nicolet, Y., Lockridge, O., Masson, P., Fontecilla-Camps, J. C., and Nachon, F. (2003) Crystal structure of human butyrylcholinesterase and of its complexes with substrate and products, *J. Biol. Chem. 278*, 41141−41147.
11. Saxena, A., Redman, A. M. G., Jiang, X., Lockridge, O., and Doctor, B. P. (1997) Differences in active site gorge dimensions of cholinesterases revealed by binding of inhibitors to human butyrylcholinesterase, *Biochemistry 36*, 14642−14651.
12. Fersht, A. R. (1995) *Enzyme Structure and Mechanism*, W. H. Freeman and Co., New York.
13. Masson, P., Nachon, F., Bartels, C. F., Froment, M.-T., Ribes, F., Matthews, C., and Lockridge, O. (2003) High activity of human butyrylcholinesterase at low pH in the presence of excess butyrylthiocholine, *Eur. J. Biochem. 270*, 315−324.
14. Stojan, J., Golicnik, M., Froment, M.-T., Estour, F., and Masson, P. (2002) Concentration-dependent reversible activation-inhibition of human butyrylcholinesterase by tetraethylammonium ion, *Eur. J. Biochem. 269*.
15. Masson, P., Cléry, C., Guerra, P., Redslob, A., Albaret, C., and Fortier, P.-L. (1999) Hydration change during the aging of phosphorylated human butyrylcholinesterase: Importance of residues aspartate-70 and glutamate-197 in the water network as probed by hydrostatic osmotic pressures, *Biochem. J. 343*, 361−369.
16. Masson, P., Froment, M.-T., Bartels, C. F., and Lockridge, O. (1996) Asp70 in the peripherical anionic site of human butyrylcholinesterase, *Eur. J. Biochem. 235*, 36−48.
17. Koellner, G., Steiner, T., Millard, C. B., Silman, I., and Sussman, J. L. (2002) A neutral molecule in a cation-binding site: Specific binding of a PEH−SH to acetylcholinesterase from *Torpedo californica*, *J. Mol. Biol. 320*, 721−725.
18. Harel, M., Kryger, G., Rosenberry, T. L., Mallender, W. D., Lewis, T., Fletcher, R. J., Guss, J. M., Silman, I., and Sussman, J. (2000) Three-dimensional structures of *Drosophila melanogaster* acetylcholinesterase and of its complexes with two potent inhibitors, *Protein Sci. 9*, 1063−1072.
19. Bourne, Y., Taylor, P., Radic, Z., and Marchot, P. (2003) Structural insights into ligand interactions at the acetylcholinesterase peripehral anionic site, *EMBO J. 22*, 1−12.
20. Hurley, M. M., Wright, J. B., Lushington, G. H., and White, W. E. (2003) Quantum mechanics and mixed quantum mechanics/molecular mechanics simulations of model nerve agents with acetylcholinesterase, *Theor. Chem. Acc. 109*, 160−168.

21. Bui, J. M., Henchman, R. H., and McCammon, J. A. (2003) The dynamics of ligand barrier crossing inside the acetylcholinesterase gorge, *Biophys. J. 85*, 2267−2272.
22. Tai, K., Shen, T., Börjesson, U., Philippopoulos, M., and McCammon, J. A. (2001) Analysis of a 10-ns molecular dynamics simulation of mouse acetylcholinesterase, *Biophys. J. 81*, 715−724.
23. Wlodek, S. T., Clark, T. W., Scott, L. R., and McCammon, J. A. (1997) Molecular dynamics of acetylcholinesterase dimer complexed with tacrine, *J. Am. Chem. Soc. 119*, 9513−9522.
24. Fuxreiter, M., and Warshel, A. (1998) Origin of the catalytic power of acetylcholinesterase: Computer simulation studies, *J. Am. Chem. Soc. 120*, 183−194.
25. Vagedes, P., Rabenstein, B., Aqvist, J., Marelius, J., and Knapp, E.-W. (2000) The deacylation step of acetylcholinesterase: Computer simulation studies, *J. Am. Chem. Soc. 122*, 12254−12262.
26. Zhang, Y., Kua, J., and McCammon, J. A. (2002) Role of the catalytic triad and oxyanion hole in acetylcholinesterase catalysis: An ab initio QM/MM study, *J. Am. Chem. Soc. 124*, 10572−10577.
27. Zhang, L., Kua, J., and McCammon, J. A. (2003) Influence of structural fluctuation on enzyme reaction energy barriers in combined quantum mechanical/molecular mechanical studies, *J. Phys. Chem. B 107*, 4449−4463.
28. Zhan, C.-G., Zheng, F., and Landry, D. W. (2003) Fundamental reaction mechanism for cocaine hydrolysis in human butyrylcholinesterase, *J. Am. Chem. Soc. 125*, 2462−2474.
29. Zhan, C.-G., and Gao, D. (2005) Catalytic mechanism and energy barriers for butyrylcholinesterase-catalyzed hydrolysis of cocaine, *Biophys. J. 89*, 3863−3872.
30. Becke, A. D. (1995) Exchange-correlation approximation in density-functional theory, in *Modern Electronic Structure Theory Part II* (Yarkony, D. R., Ed.) World Scientific, Singapore.
31. (1991−2003) *JAGUAR*, Schrödinger, L.LC., Portland, OR.
32. Frisch, M. J., Trucks, G. W., Schlegel, H. B., Scuseria, G. E., Robb, M. A., Cheeseman, J. R., Montgomery, J. A., Jr., Vreven, T., Kudin, K. N., Burant, J. C., Millam, J. M., Iyengar, S. S., Tomasi, J., Barone, V., Mennucci, B., Cossi, M., Scalmani, G., Rega, N., Petersson, G. A., Nakatsuji, H., Hada, M., Ehara, M., Toyota, K., Fukuda, R., Hasegawa, J., Ishida, M., Nakajima, T., Honda, Y., Kitao, O., Nakai, H., Klene, M., Li, X., Knox, J. E., Hratchian, H. P., Cross, J. B., Bakken, V., Adamo, C., Jaramillo, J., Gomperts, R., Stratmann, R. E., Yazyev, O., Austin, A. J., Cammi, R., Pomelli, C., Ochterski, J. W., Ayala, P. Y., Morokuma, K., Voth, G. A., Salvador, P., Dannenberg, J. J., Zakrzewski, V. G., Dapprich, S., Daniels, A. D., Strain, M. C., Farkas, O., Malick, D. K., Rabuck, A. D., Raghavachari, K., Foresman, J. B., Ortiz, J. V., Cui, Q., Baboul, A. G., Clifford, S., Cioslowski, J., Stefanov, B. B., Liu, G., Liashenko, A., Piskorz, P., Komaromi, I., Martin, R. L., Fox, D. J., Keith, T., Al-Laham, M. A., Peng, C. Y., Nanayakkara, A., Challacombe, M., Gill, P. M. W., Johnson, B., Chen, W., Wong, M. W., Gonzalez, C., and Pople, J. A. (2004) Gaussian, Inc., Wallingford, CT.
33. Tannor, D. J., Marten, B., Murphy, R., Friesner, R. A., Sitkoff, D., Nicholls, A., Ringnalda, M., Goddard, I., W. A., and Honig, B. (1994) Accurate first principles calculation of molecular charge distributions and solvation energies from ab initio quantum mechanics and continuum dielectric theory, *J. Am. Chem. Soc. 116*, 11875−11882.
34. Bader, R. F. W. (1990) *Atoms in Molecules: A Quantum Theory (the International Series on Monographs on Chemistry; 22)*, Oxford University Press, Oxford, U.K.
35. Biegler-König, F. W., Bader, R. F. W., and Wang, T. H. (1982) Calculation of the average properties of atoms in molecules. II, *J. Comput. Chem. 3*, 317−328.
36. Sham, Y. Y., Chu, Z. T., Tao, H., and Warshel, A. (2000) Examining methods for calculations of binding free energies: LRA, LIE, PDLP−LRA, and PDLP/S-LRA calculations of ligands binding to an HIV protease, *Proteins: Struct., Funct., Genet. 39*, 393−407.
37. Kollman, P. A., Massova, I., Reyes, C., Kuhn, B., Huo, S., Chong, L., Lee, M., Lee, T., Duan, Y., Wang, W., Donini, O., Cieplak, P., Srinivasan, J., Case, D. A., and Cheatham, T. E. (2000) Calculating structures and free energies of complex molecules: Combining molecular mechanics and continuum models, *Acc. Chem. Res. 33*, 889−897.
38. Gohlke, H., and Case, D. A. (2003) Converging free energy estimates: MM−PB(GB)SA studies on the protein−protein complex RAS−RAF, *J. Comput. Chem. 25*, 238−250.
39. Cornell, W. D., Cieplak, P., Bayly, C. I., Gould, I. R., Merz, K. M., Jr., Ferguson, D. M., Spellmeyer, D. C., Fox, T., Caldwell, J. W., and Kollman, P. A. (1995) A second generation force field for the simulation of proteins, nucleic acids, and organic molecules, *J. Am. Chem. Soc. 117*, 5179−5197.
40. Antosiewicz, J., McCammon, J. A., and Gilson, M. K. (1994) Prediction of pH-dependent properties of proteins, *J. Mol. Biol. 238*, 415−436.
41. Elber, R. (1990) Calculation of the potential of mean force using molecular dynamics with linear constraints: An application to a conformational transition in a solvated peptide, *J. Chem. Phys. 93*, 4312−4321.
42. Elber, R., and Karplus, M. (1990) Enchanced sampling in molecular dynamics. Use of the time dependent hartree approximation for a simulation of carbon monoxide diffusion through myoglobin, *J. Am. Chem. Soc.*, 9161−9175.
43. Bayly, C. A., Cieplak, P., Cornell, W. D., and Kollman, P. A. (1993) A well behaved electrostatic potential based method using charge restraints for deriving atomic charges: The resp model, *J. Phys. Chem. 97*, 10269−10280.
44. Suárez, D., and Field, M. J. (2005) Molecular dynamics simulations of human butyrylcholinesterase, *Proteins: Struct., Funct., Bioinf. 59*, 104−117.
45. Case, D. A., Pearlman, D. A., Caldwell, J. W., Cheatham, T. E., II, Ross, W. S., Simmerling, C. L., Darden, T. A., Merz, K. M., Jr., Stanton, R. V., Cheng, A. L., Vincent, J. J., Crowley, M., Ferguson, D. M., Radmer, R. J., Seibel, G. L., Singh, U. C., Weiner, P. K., and Kollman, P. A. (2002) AMBER 7.0, University of California, San Francisco, CA.
46. Sharp, K., and Honig, B. (1991) Electrostatic interactions in macromolecules: Theory and applications, *Annu. Rev. Biophys. Biophys. Chem. 19*, 301−332.
47. Rocchia, W., Alexov, E., and Honig, B. (2001) Extending the applicability of the nonlinear Poisson−Boltzmann equation: Multiple dielectric constants and multivalent ions, *J. Phys. Chem. B 105*, 6507−6514.
48. Rappé, A. K., Casewit, C. J., Colwell, K. S., Goddard, W. A., III, and Skiff, W. M. (1992) UFF, a full periodic table force field for molecular mechanics and molecular dynamics simulations, *J. Am. Chem. Soc. 114*, 10024−10035.
49. Bone, R. G. A., and Bader, R. F. W. (1996) Identifying and analyzing intermolecular bonding interactions in van der Waals molecules, *J. Phys. Chem. 100*, 10892−10911.

BI052176P